




Infrared response in photocatalytic polymeric carbon nitride for water splitting via an upconversion mechanism

Zhengyuan Jin ^{1,2,3}, Xiantao Jiang², Qitao Zhang², Shaolong Huang¹, Luhong Zhang¹, Lili Huang³, Tingchao He¹, Han Zhang ², Teruhisa Ohno⁴, Shuangchen Ruan¹ & Yu-Jia Zeng ¹✉

Broad-spectrum light activation in photocatalytic materials is considered vital for effective solar-to-hydrogen energy conversion. Here, we propose an upconversion process in oxygen-doped polymeric carbon nitride (C_3N_4) nanosheets, resulting in high photocatalytic activity for hydrogen generation from water splitting under infrared light irradiation. Due to the upconversion, the photoexcited electrons are transferred to the conduction band, and a σ^* carbon-oxygen orbital localized on the triazine matrix ring resulting from oxygen doping extends the lifetime of photogenerated electrons, which increases the photocatalytic activity under both infrared and visible light. Our material exhibits high apparent quantum efficiency of 0.014% and 23% at 850 nm and 420 nm, respectively. Under infrared light ($\lambda \geq 800$ nm, 24 mW cm^{-2}), the hydrogen production rate of our material is $22.84 \mu\text{mol h}^{-1} \text{g}^{-1}$, which can reach a yield similar to that of pristine C_3N_4 under visible light.

¹Shenzhen Key Laboratory of Laser Engineering, College of Physics and Optoelectronic Engineering, Shenzhen University, Shenzhen 518060, P. R. China.

²Shenzhen Engineering Laboratory of Phosphorene and Optoelectronics, International Collaborative Laboratory of 2D Materials for Optoelectronics Science and Technology, Shenzhen University, Shenzhen 518060, P. R. China. ³Ctr Adv Mat Diagnost Technol, Shenzhen Technol University, Shenzhen 518118, P. R. China. ⁴Department of Applied Chemistry, Faculty of Engineering, Kyushu Institute of Technology, 1-1 Sensuicho, Tobata, Kitakyushu 804-8550, Japan.

✉email: yjzeng@szu.edu.cn

Photocatalysis is considered one of the most promising technologies for converting abundantly available solar energy into useful chemical energy. In particular, solar-driven water splitting for H₂ generation has attracted much attention because it is a sustainable strategy for producing renewable energy^{1,2}. However, the low utilization efficiency for solar energy is still a bottleneck in photocatalysis because photocatalysts typically have a narrow absorption range. For example, TiO₂, the most well-studied photocatalyst, can respond only to ultraviolet light (5% of total solar energy)³. The theoretical maximum efficiency for the water splitting reaction by a single photocatalyst increases with the wavelength; i.e., values of 2, 16, and 32% are obtained upon increasing the wavelength from UV to 400, 600, and 800 nm, respectively^{4,5}. Therefore, to improve the solar energy utilization efficiency, developing a photocatalyst with broad-spectrum responsiveness is one of the most effective strategies for solar-to-hydrogen energy conversion. Theoretically, the water splitting reaction can proceed only in a photocatalyst whose band gap straddles the reduction and oxidation potentials of water. It is, therefore, a great challenge to find a good material that simultaneously has a broad-spectrum response and suitable redox potentials. Neither new materials such as black phosphorus (phosphene) nor TiO_{2-x} obtained from band gap engineering has achieved the desired photocatalytic activity due to the low redox capacity of these materials^{6,7}.

We propose a different strategy to design infrared light-responsive photocatalysts. The strategy is based on a single photocatalyst in which the infrared light response is achieved by an upconversion process and high activity is guaranteed by the prolonged lifetime of the photoexcited carriers achieved by the introduction of a new energy level in conduction band. Polymeric carbon nitride (C₃N₄) has been one of the most popular materials in photocatalysis in the past decade since its discovery as a visible light-responsive photocatalyst in 2009⁸. However, C₃N₄ has never been applied as an infrared light-responsive material or an upconversion material, despite very limited reports on its upconversion properties, which have been ascribed to the quantum size effect^{9,10}. Herein, we demonstrate that upconversion, which we believe is an important but overlooked process, is an “intrinsic” process even in bulk C₃N₄ (PCN).

In this work, when the weight ratio of melamine to cyanuric acid reaches M/C ≤ 1/3, we obtain a carbon nitride in the form of porous nanosheets, in which O is doped at the position of the triazine matrix ring to form a new energy level in conduction band. We find the energy level provided by σ*_{C-O} in the conduction band, which is beneficial for prolonging the life time of photogenerated electrons. Moreover, σ*_{C-O} is next to π*_{C=N-C}, which makes the electrons easy to be photogenerated to the level even by infrared light (two-photon absorption). Therefore, our carbon nitride not only generates H₂ from water splitting under infrared light irradiation, but also the H₂ generation rate of MCN1-4 under visible light irradiation is 85.7 times higher than that of PCN.

Results

Characterization of PCN and MCN1-4. The texture, structure, and morphology of the samples were investigated by scanning electron microscopy (SEM), transmission electron microscopy (TEM) and atomic force microscopy (AFM). PCN shows large particles with a stacked sheet structure (Fig. 1a, b). On the other hand, MCN1-4 shows a translucent thin layer morphology with a porous surface and folded edges (Fig. 1c, d). As shown in the AFM image (Fig. 1e), the nanosheets of MCN1-4 have an average thickness of approximately 3.5 nm and an average planar area of ~18 μm². MCN1-4 has a Brunauer-Emmett-Teller (BET) specific

surface area of 150.0 m² g⁻¹, which is 14 times higher than that of PCN (11.3 m² g⁻¹), indicating that most MCN1-4 samples exhibit an ultra-thin nanosheet morphology (see Supplementary Table 1). The total Barrett-Joyner-Halenda (BJH) pore volume of MCN1-4 is up to 0.79 cm³ g⁻¹, which is almost 8 times higher than that of PCN (0.10 cm³ g⁻¹). Notably, MCN1-4 has a microporous structure (0.02 cm³ g⁻¹), which not only provides a number of reaction sites, but also decreases the charge transfer distance and thus effectively increases the photocatalytic activity (see Supplementary Fig. 6c)

Figure 2a shows X-ray diffraction (XRD) patterns of PCN and MCN1-4 samples. PCN has two peaks at 13.1 degrees and 27.6 degrees, which are assigned to in-plane repeating units (100) of the tri-s-triazine matrix and the interlayer distances of parallel conjugated aromatics (002), respectively¹¹. The characteristic peaks of MCN1-4 are located at 13.1 degrees and 27.8 degrees, indicating that MCN1-4 has the same structure as PCN. The most intense peak of MCN1-4 shifts slightly to 27.8 degrees, suggesting that MCN1-4 has a shorter stacking interlayer distance (0.3206 nm) than does PCN (0.3232 nm). Simultaneously, the peak at 27.8 degrees becomes less pronounced, indicating that the number of layers in the structure is reduced to form a thinner structure¹², which agrees with the morphology results presented in Fig. 1. Both the reduction in the interlayer distance and the nanosheet morphology are beneficial to increasing the lifetime of photoexcited carriers to enhance photocatalytic activity.

To further identify the functional groups of molecules, Fourier transform infrared (FT-IR) spectroscopy was employed (Fig. 2b). Both samples give rise to a peak characteristic of the tri-s-triazine ring mode at approximately 806.1 cm⁻¹. The MCN1-4 spectrum presents several new peaks from 1238 and 1070 cm⁻¹, which are assigned to stretching vibrations of the C-O-C group^{13,14}. The bands between 1700 and 1200 cm⁻¹ are attributed to the skeletal stretching vibration of aromatic C-N heterocycles. These peaks in the spectrum of MCN1-4 shift to lower wavenumbers than those of PCN, which may be due to the presence of a C-O-C moiety. No significant changes are detected in the peaks at 3100–3300 cm⁻¹ (see Supplementary Fig. 7b), which correspond to -NHx moieties. The FT-IR results confirm the O doping in the C₃N₄.

To further elucidate the O doping position, the chemical states of elements were studied by X-ray photoelectron spectroscopy (XPS). As shown in the XPS survey spectra (see Supplementary Fig. 8), MCN1-4 is composed of C, N, and O, similar to PCN. The C1s XPS spectrum of PCN shows two fitting peaks at 284.6 and 288.0 eV, corresponding to the C-C and N=C-N bonds (Fig. 2c). The spectrum of MCN1-4 shows three fitting peaks, including a new peak at 286.2 eV attributed to the C-O bond¹³. Figure 2d shows the O1s XPS spectra of the samples. The spectra of both samples show a peak at 532.0 eV, which is ascribed to chemisorbed oxygen (H₂O). Note that the spectrum of MCN1-4 has a new peak at approximately 533.2 eV, which is attributed to the C-O-C moiety¹⁴. In the C₃N₄ structure, C-O-C may exist in two positions: at the linker position N_(-NHx) and at the triazine matrix ring N_(C=N-C). As shown in Fig. 2e, the N1s spectra of the two samples exhibit three fitted peaks at 398.5, 399.6, and 401.0 eV, which are attributed to C=N-C, N-(C)₃ and C-NHx, respectively. For PCN, the ratios of the N1_(C=N-C), N2_(N-C₃) and N3_(-NHx) peaks are 66%, 28%, and 6%, respectively, but the ratios of these three peaks in MCN1-4 are 59%, 32%, and 9% (see Supplementary Tables 4–6)¹⁵. Only the ratio of N1 (C=N-C) decreased, indicating that the O atom of C-O-C is located at the N position of the triazine matrix ring in MCN1-4.

The results of elemental analysis (EA) and XPS elemental analysis (XPS-EA) are shown in Supplementary Tables 2 and 3 and illustrate the distribution of the elements. The surface O ratio of MCN1-4 is 28% and 9% higher than that of PCN, as seen from

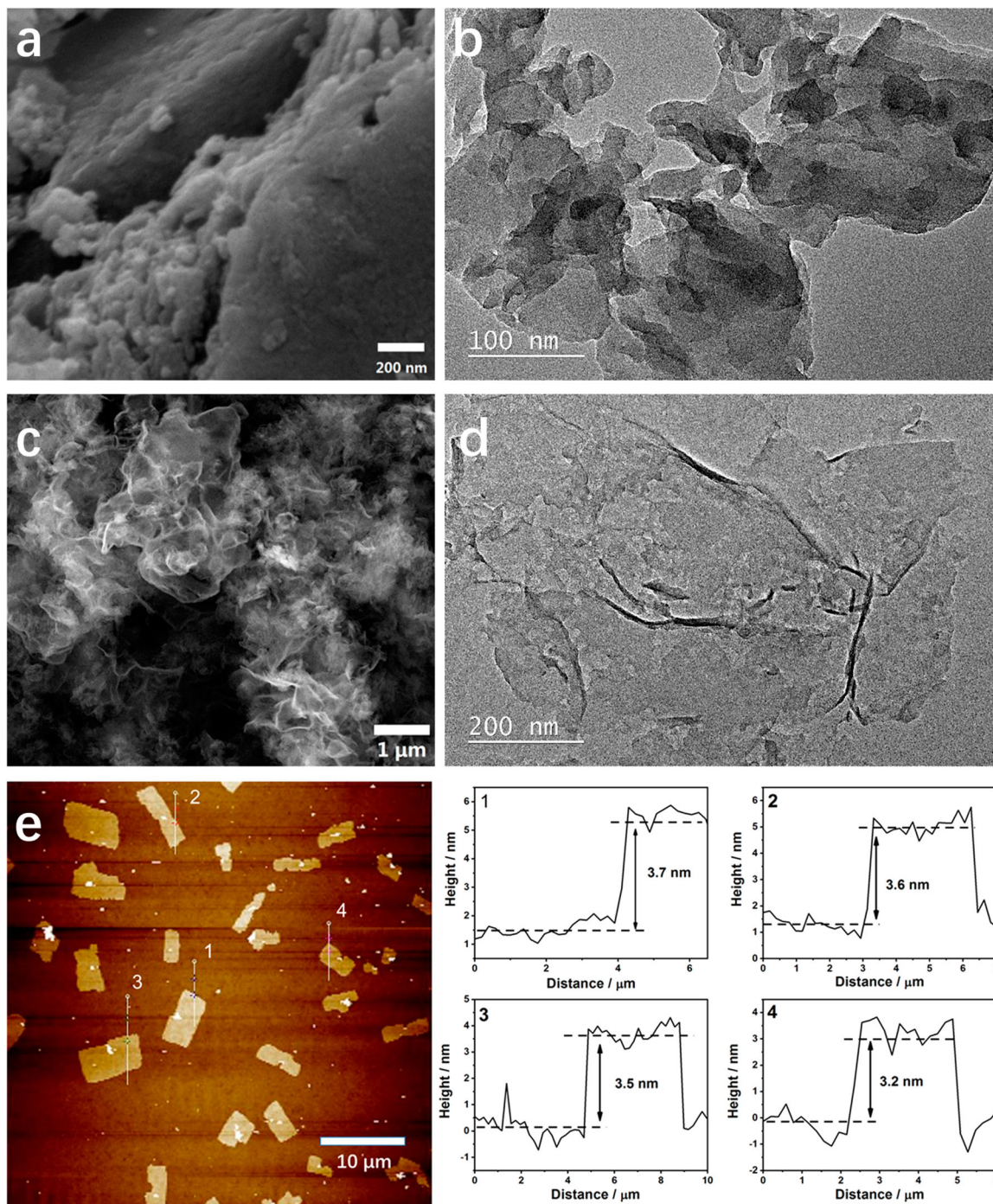


Fig. 1 Structure of PCN and MCN1-4. **a, c** SEM images of PCN and MCN1-4; **b, d** TEM images of PCN and MCN1-4; **e** AFM image and the corresponding height profiles of MCN1-4.

the XPS-EA and EA results, respectively; these results indicate that C–O–C is mainly distributed on the surface of MCN1-4, since XPS is more surface sensitive. Compared with the surface C/N ratio of PCN, that of MCN1-4 increases, but the overall C/N ratio decreases. The results show that the C content gradually increases from the inside to the surface of MCN1-4¹⁶, which is beneficial for charge transfer from the inside to the surface.

Electron paramagnetic resonance (EPR) spectra of the samples are shown in Fig. 2f. The spectra of both samples exhibit an isotropic singlet with a Lorentzian line shape at $g = 2.0042$, which is assigned to the lone pair electrons of the sp^2 -hybridized carbons in the π -bonded aromatic rings¹⁷. The peak intensity of

MCN1-4 is lower than that of PCN, indicating a decrease in the unpaired electron density. This finding is probably due to the replacement of N with O on the triazine matrix ring, which partially destroys the π bonding structure of the entire ring.

Solid-state NMR (nuclear magnetic resonance) was used to verify the structure of the surface species (Fig. 3a, b). For PCN, the ^{13}C magic-angle spinning (MAS) NMR spectrum shows two peaks at 156.7 and 164.7 ppm, which can be assigned to $(\text{C})_3\text{N}$ and $(\text{C})_2\text{N-NHx}$ ¹⁸, the ^1H MAS NMR spectrum shows two peaks at 4.5 and 9.6 ppm^{19,20}, which can be ascribed to R–NH₂ and R–NH–R, respectively. MCN1-4 presents new peaks at 163.3 and 3.4 ppm in the ^{13}C and ^1H MAS NMR spectra, respectively,

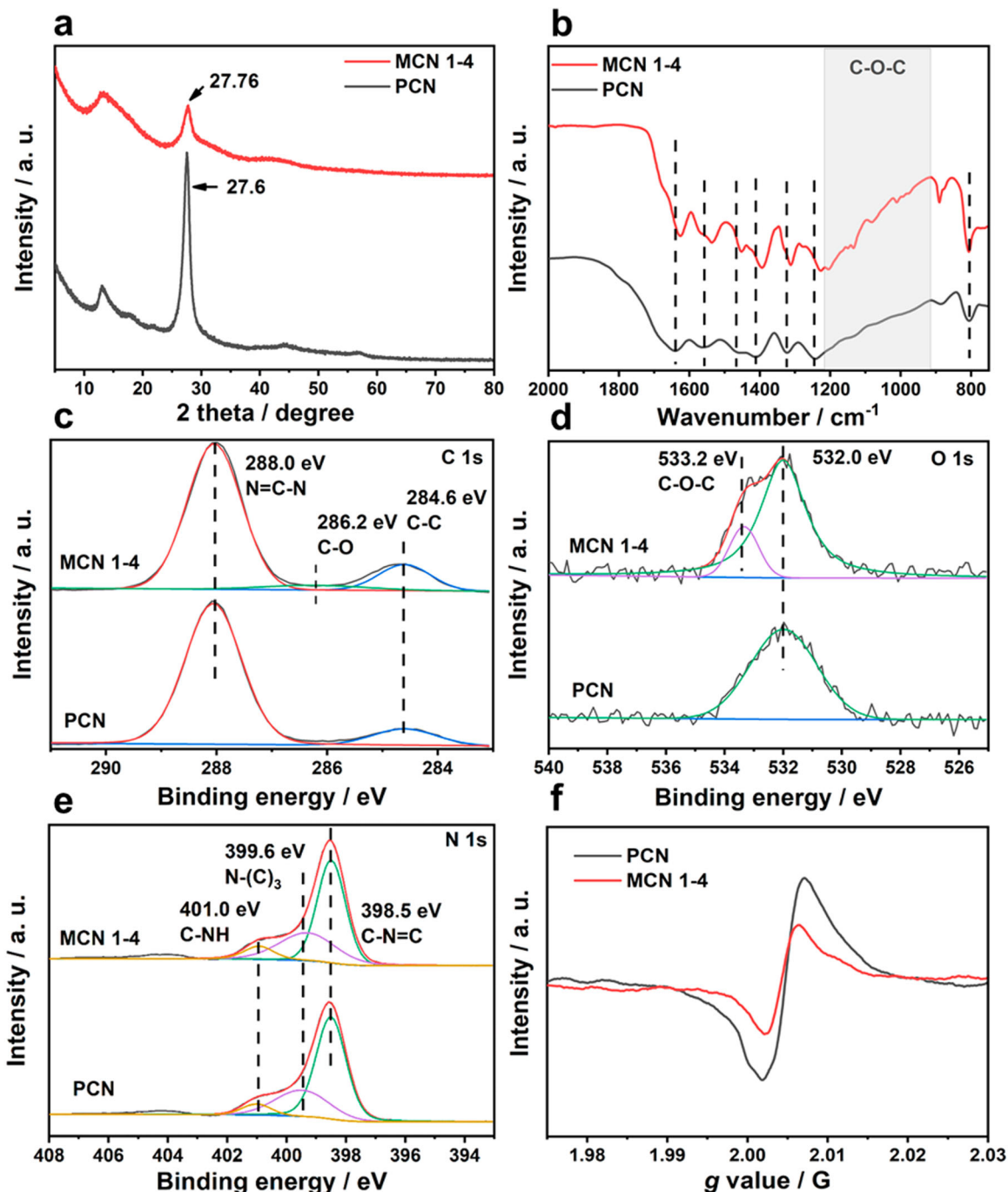


Fig. 2 XRD, FT-IR, and EPR characterization of PCN and MCN1-4. **a** XRD patterns, **b** FT-IR spectra, **c** C1s XPS spectra, **d** O1s XPS spectra, **e** N1s XPS spectra, and **f** in situ EPR signals of PCN and MCN1-4.

in addition to the peaks at the same positions as those for PCN. The peaks at 163.3 ppm and 3.4 ppm are attributed to $-\text{O}-\text{CN}$ and $-\text{CH}-\text{O}-$ (according to the database “Chem 605” provided by Hans J. Reich, University of Wisconsin.), respectively, indicating the presence of $\text{C}-\text{O}-\text{C}$ in the triazine matrix ring of MCN1-4 (inset of Fig. 3b). Since the oxygen in $\text{C}-\text{O}-\text{C}$ has two lone pairs of electrons, the other peaks shift downfield, which is consistent with the EPR results.

A schematic illustration of the formation of O-doped porous nanosheet carbon nitride is shown in Fig. 3c. Hydrothermal treatment of the appropriate weight ratio of melamine and cyanuric acid results in O doping in the triazine matrix ring to replace $\text{N}_{(\text{C}-\text{N}=\text{C})}$. Moreover, we find that the M/C weight ratio of

$1/3$ is the key point, as shown in Supplementary Fig. 13. Because a melamine molecule can form hydrogen bonds with three cyanuric acids^{21,22}, when melamine is surrounded by cyanuric acid, spatial distance will exist between melamine molecules, which results in the formation of the O-doped porous nanosheet morphology.

Photocatalytic activities. Figure 4a shows the time course of H_2 generation from water splitting under infrared light ($\lambda \geq 800 \text{ nm}$) irradiation. PCN catalyses no H_2 production, whereas MCN1-4 generates $4.27 \mu\text{mol}$ of H_2 after 4 h of irradiation (generation rate of $22.84 \mu\text{mol h}^{-1} \text{g}^{-1}$). Considering that the intensity of infrared light is only 24.4 mW cm^{-2} , the photocatalytic activity of MCN1-4 exhibits even higher under 100 mW cm^{-2} of infrared light than

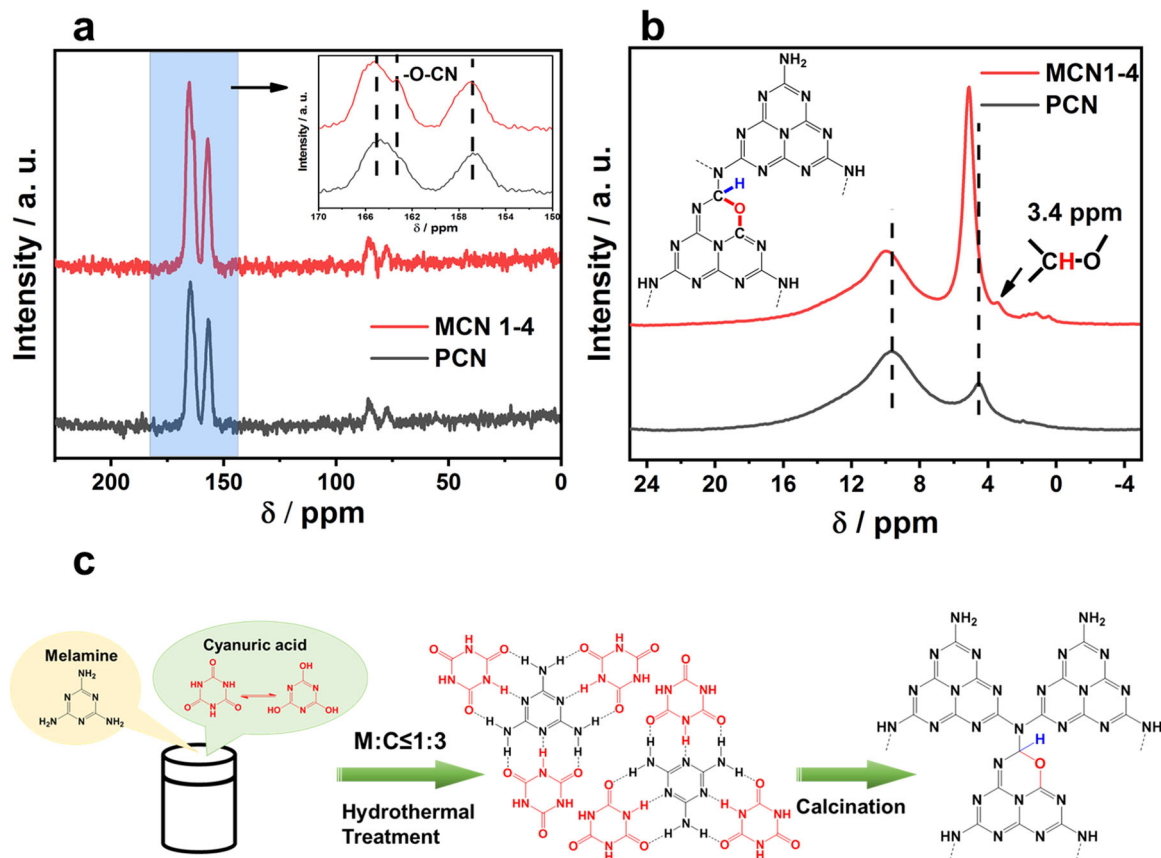


Fig. 3 NMR characterization and fabrication process of MCN1-4. **a** ^{13}C and **b** ^1H NMR solid-state spectra of PCN and MCN1-4. **c** Schematic illustration of the formation of O-doped two-dimensional carbon nitride.

that of PCN under visible light ($37.09 \mu\text{mol h}^{-1} \text{g}^{-1}$) as shown in Supplementary Fig. 14.

Figure 4b shows the photoluminescence (PL) spectra of PCN and MCN1-4 upon excitation at 800 nm. The PL spectra of both samples show a peak in the blue region (450–500 nm), indicating that the samples have upconversion properties²³. The PL spectra together with time-resolved fluorescence decay spectra are used to evaluate the charge separation dynamics of the samples. PCN gives rise to a peak centred at 468 nm, and MCN1-4 gives rise to a peak centred at 496 nm. The peak intensity in the spectrum of MCN1-4 is lower than that in the spectrum of PCN, demonstrating that MCN1-4 has a lower recombination rate of photoexcited carriers. Furthermore, MCN1-4 has a much longer average lifetime of 7.63 ns than does PCN, with an average lifetime of 4.41 ns (see Supplementary Fig. 15 and Supplementary Table 7). In the case of PCN, the short average lifetime of 4.41 ns and the stacked sheet structure prevent the photoexcited carrier from being transferred from the interior of the material to the reaction site on the surface. Therefore, although electrons are photoexcited to the conduction band of PCN, the lifetime of the excited state is too short for water splitting to proceed. In contrast, MCN1-4 exhibits a long lifetime of 7.63 ns (almost the same as the average lifetime at 365 nm) and a porous nanosheet (3.5 nm) structure; thus, photoexcited electrons have a sufficient lifetime for water splitting. As shown in Fig. 4c, when PCN is excited with an 800 nm laser, white light can be clearly observed from the material even at a laser pump power of $\sim 100 \text{ mW cm}^{-2}$. On the other hand, little light can be observed from MCN1-4 under the same condition, which is consistent with the results of PL. Nonlinear optical characteristics can be found from the intensity-dependent fluorescence spectra of MCN1-4 excited at

800 nm. Moreover, it is found that the hydrogen generation rate is proportional to the irradiation intensity (slope = 1.77), thus confirming the existence of two-photon absorption (2PA) mechanism at inferred light ($\lambda \geq 800 \text{ nm}$, see Supplementary Fig. 16). The nonlinear absorption coefficients (two-photon absorption coefficient) of PCN and MCN1-4 are $0.9696 \times 10^{-2} \text{ cm GW}^{-1}$ and $6.26 \times 10^{-2} \text{ cm GW}^{-1}$, respectively, which are calculated from the results of open-aperture Z-scan under 800 nm excitation (see Supplementary Fig. 17)²⁴.

The photocatalytic activities under visible light were measured by in situ H_2 generation from water splitting. After 6 h of irradiation under visible light ($\lambda \geq 420 \text{ nm}$), MCN1-4 generates $179.44 \mu\text{mol}$ of H_2 , while PCN generates $1.61 \mu\text{mol}$ (Fig. 4d). Part of the photoexcited electrons are used to reduce the Pt^{4+} available at the beginning of the experiment, resulting in a decrease in the hydrogen production²⁵. Thus, the average H_2 generation rate is calculated between 3 and 6 h, during which time the hydrogen production rate tends to be stable. The average H_2 generation rates of MCN1-4 and PCN are $31.79 \mu\text{mol h}^{-1}$ and $0.37 \mu\text{mol h}^{-1}$, respectively; i.e., the value for MCN1-4 is 85.7 times higher than that for PCN (Fig. 4h).

Figure 4e shows the PL spectra of PCN and MCN1-4 upon excitation at 365 nm, which are similar to those obtained upon 800 nm excitation. The PL peak intensity of MCN1-4 is lower than that of PCN, and the average lifetime of MCN1-4 (7.84 ns) is longer than that of PCN (6.83 ns), confirming the lower recombination rate of photoexcited carriers in MCN1-4 than in PCN (see Supplementary Fig. 15 and Supplementary Table 8). On the other hand, the PL peaks in the PCN spectrum are at the same position after excitation at both 365 and 800 nm. However, the MCN1-4 spectrum shows three distinct peaks with different

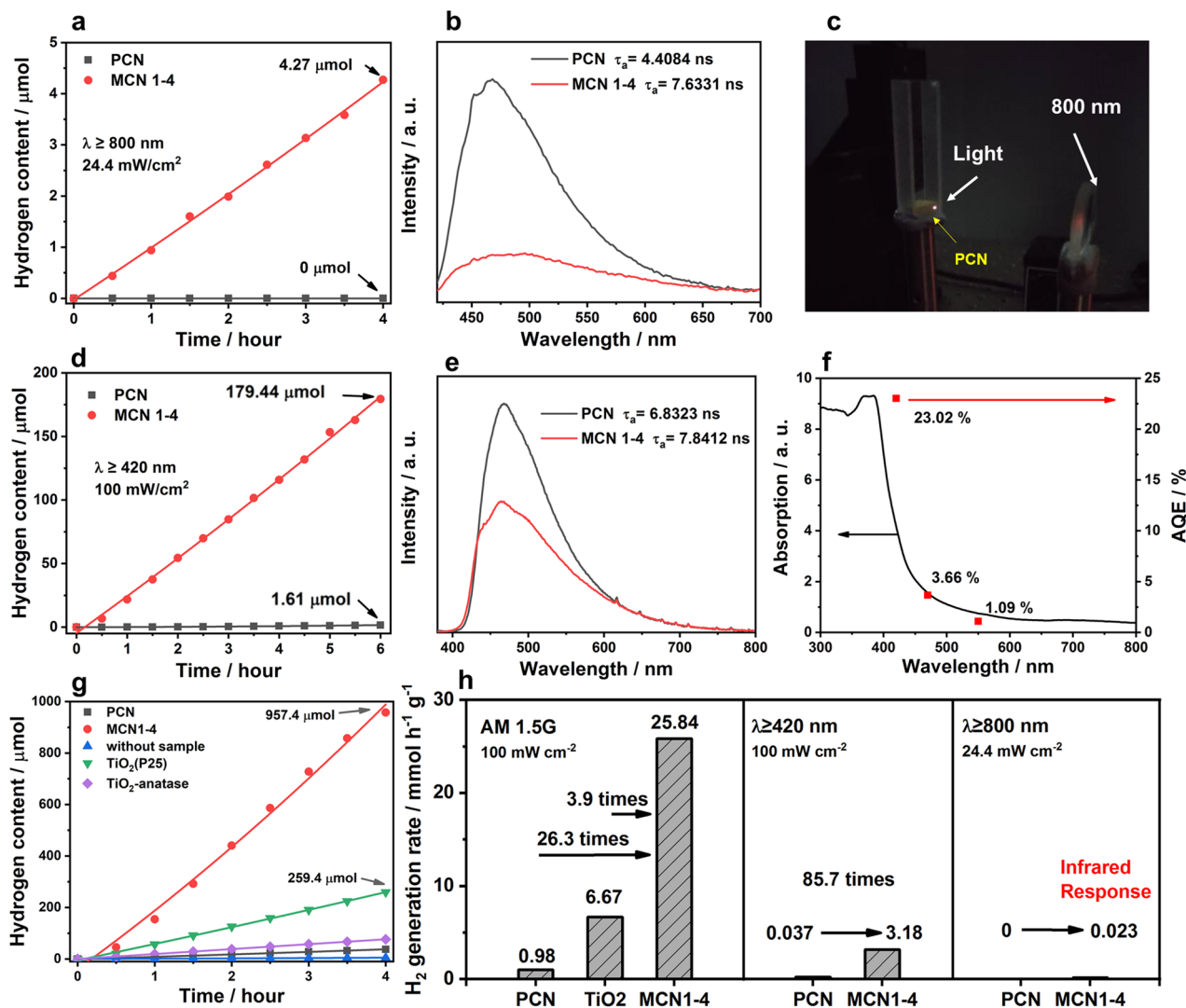


Fig. 4 Photocatalytic H₂ production performance over the samples under irradiation of various light source and characterization of PL. **a** Time course of H₂ generation from water splitting under infrared light ($\lambda \geq 800$ nm) irradiation, **b** steady-state PL spectra with 800 nm excitation, **c** digital photograph of light emission from PCN under 800 nm laser excitation, **d** time course of H₂ generation from in situ water splitting under visible light ($\lambda \geq 420$ nm) irradiation, **e** steady-state PL spectra upon 365 nm excitation, **f** AQE against the light absorption wavelength of the H₂ generation rate of MCN1-4, **g** time course of H₂ generation from in situ water splitting under AM 1.5 irradiation, **h** the H₂ generation rate of samples at different light sources irradiation.

excitation wavelengths, indicating that MCN1-4 has a more complex band structure (see Supplementary Fig. 18), which will be discussed in the next section.

AQE is one of the most important parameters used to compare the photocatalytic activities of different materials²⁶. MCN1-4 presents an AQE of 23.02% under monochromatic 420 nm light irradiation, which is one of the highest recorded values for C₃N₄. In addition, MCN1-4 still has AQEs of 3.66% and 1.09% under monochromatic 470 nm and 550 nm light irradiation, respectively, indicating that this material has a broad photoresponse. (see Supplementary Fig. 19).

Figure 4g shows the time course of H₂ generation from water splitting under AM 1.5 G irradiation. Although TEOA is unstable and generate H₂ under ultraviolet light irradiation, it can be ignored because the yield of H₂ is very low (4.9 μmol in 6 h). Under the AM1.5 G irradiation, the H₂ generation rate of MCN1-4 is 25.84 $\text{mmol h}^{-1} \text{g}^{-1}$, which is four times higher than that of TiO₂ (P25), becoming the first carbon nitride material to surpass P25 and also becomes the full spectrum response carbon nitride without hybridization (Fig. 4h)²⁷.

The stability of MCN1-4 was measured by photocatalytic reaction over 36 h of visible light irradiation (see Supplementary Fig. 20). During visible light irradiation, the photocatalytic activity hardly changes in the first 18 h. The activity decreases by ~8% in the third cycle (24–30 h). After adding 5 ml of triethanolamine (TEOA), the activity is slightly higher than that in the first cycle (0–6 h). This change in activity is mainly due to a change in the pH of the solution because TEOA is an alkaline substance. The recovery of activity indicates that MCN1-4 has good stability.

To understand the band structures of the materials, we performed UV-visible diffuse-reflectance spectroscopy (UV-vis DRS), valence band XPS (VB-XPS) and transient absorption spectroscopy (TAS). Figure 5a and Supplementary Fig. 21 show the UV-vis DRS results of the samples. The wavelength of maximum absorbance (λ_{max}) of MCN1-4 is located at approximately 385 nm, which is blue-shifted slightly with respect to that of PCN at ~387 nm due to the quantum confinement effect caused by the morphology of the nanosheets. MCN1-4 absorbs from approximately 478 nm to 800 nm, which may originate from

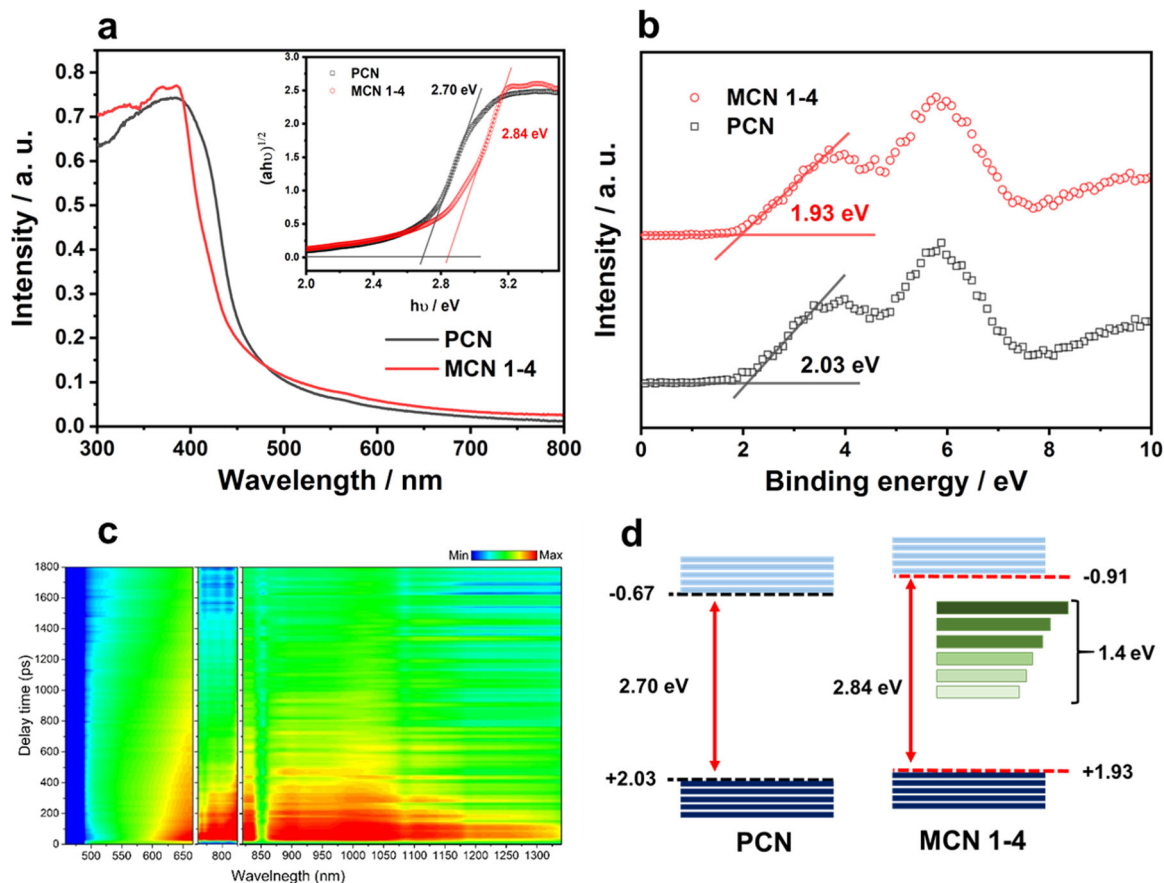


Fig. 5 UV-Vis DRS and bandgap state of PCN and MCN1-4. **a** UV-Vis DRS of PCN and MCN1-4 (the inset shows Tauc plots of samples), **b** VB-XPS spectra, **c** experimental TAS map of MCN1-4, **d** schematic band structure evolution of MCN1-4 compared with PCN.

charge transfer of the $n-\pi^*$ lone electron pairs of the O atom in the C–O–C moiety of the heptazine ring²⁸. Therefore, the energy gaps of PCN and MCN1-4 are 2.70 and 2.84 eV, respectively, according to the Kubelka–Munk equation and Tauc plot method. As seen from the VB-XPS results, the valence bands of PCN and MCN1-4 are located at 2.03 and 1.93 eV, respectively.

As determined by the TAS analysis, the actual band structure of MCN1-4 is rather complex, especially the intermediate bands. A large signal can be detected from 486 to 1081 nm (2.55 eV to 1.15 eV) in the MCN1-4 spectrum (Fig. 5c, d and see Supplementary Fig. 23), probably originating from the intermediate bands caused by the defects^{29–31}. Supplementary Fig. 23 shows the kinetics and spectral properties at different wavelengths. In the ranges of 760–820 nm and 810–1350 nm, there are many intermediate bands with lifetimes of longer than 2 ns, indicating the presence of long-wavelength ($\lambda \geq 760$ nm) sustained photoexcited electron bands (see Supplementary Fig. 24). The electrons in these bands have a sufficiently long lifetime to absorb another photon for the second excitation (Fig. 5d). For instance, in the case of 800 nm irradiation, the electrons are excited to the intermediate bands by absorbing the energy of one photon, and then the electrons absorb energy from another photon to be excited to the conduction band. We speculate based on the TAS results that MCN1-4 may respond to 1325 nm light by multiphoton absorption (see Supplementary Fig. 23h)³².

To further investigate the O-binding form, the local electronic configuration, and the chemical structure of MCN1-4, near-edge X-ray absorption fine structure (NEXAFS) analysis was used. In the nitrogen K-edge region (Fig. 6a), three main characteristic resonances are observed at 399.6, 401.7, and 402.5 eV, which

correspond to the $\pi^*_{C=N-C}$ orbitals localized on aromatic nitrogen atoms, the π^*_{N-3C} orbitals on graphitic three-coordinate nitrogen atoms, and the π^*_{N-C} orbitals of sp^3 -hybridized N–C bridging groups within the tri-s-triazine moieties, respectively. The characteristic peaks of MCN1-4 in the nitrogen K-edge region are unchanged compared to that of PCN, indicating that O is doped by substituting for the N in MCN1-4. Figure 6b shows the carbon K-edge NEXAFS spectra of PCN and MCN1-4. Both spectra have peaks at 285.7 and 288.7 eV, which are attributed to π^*_{graphite} and $\pi^*_{C=N-C}$ orbitals, respectively^{33,34}. The π^*_{graphite} and $\pi^*_{C=N-C}$ intensities of MCN1-4 are both lower than those of PCN, indicating that the interlayer π bond in MCN1-4 is stronger than that in PCN and that MCN1-4 has a thinner morphology than PCN. MCN1-4 has a new peak at 289.1 eV, which is attributed to σ^*_{C-O} of the C–O–C moiety in the triazine matrix ring³⁵. The σ^*_{C-O} (289.1 eV) orbital energy is 0.4 eV higher than that of $\pi^*_{C=N-C}$ (288.7 eV) in MCN1-4, which means that the energy level of σ^*_{C-O} is higher than the conduction band minimum³⁶. The electrons photoexcited to the σ^*_{C-O} energy level have a longer lifetime, which can be confirmed from the time-resolved PL spectrum, see Supplementary Table 7 and 8. MCN1-4 with a σ^*_{C-O} level has a lifetime of $\tau = 10.36$ ns, which is almost two times that of PCN without a σ^*_{C-O} level ($\tau = 5.52$ ns). Furthermore, under 365 nm excitation, the lifetime $\tau = 9.71$ ns for MCN1-4 is longer than that for PCN ($\tau = 8.86$ ns).

As shown in Supplementary Fig. 25, the crystal structure of MCN1-4 wrinkles by the O doping in the matrix ring, and no extra internal bands can be found from the results of calculation. Figure 7a shows total density of states (TDOS) and partially

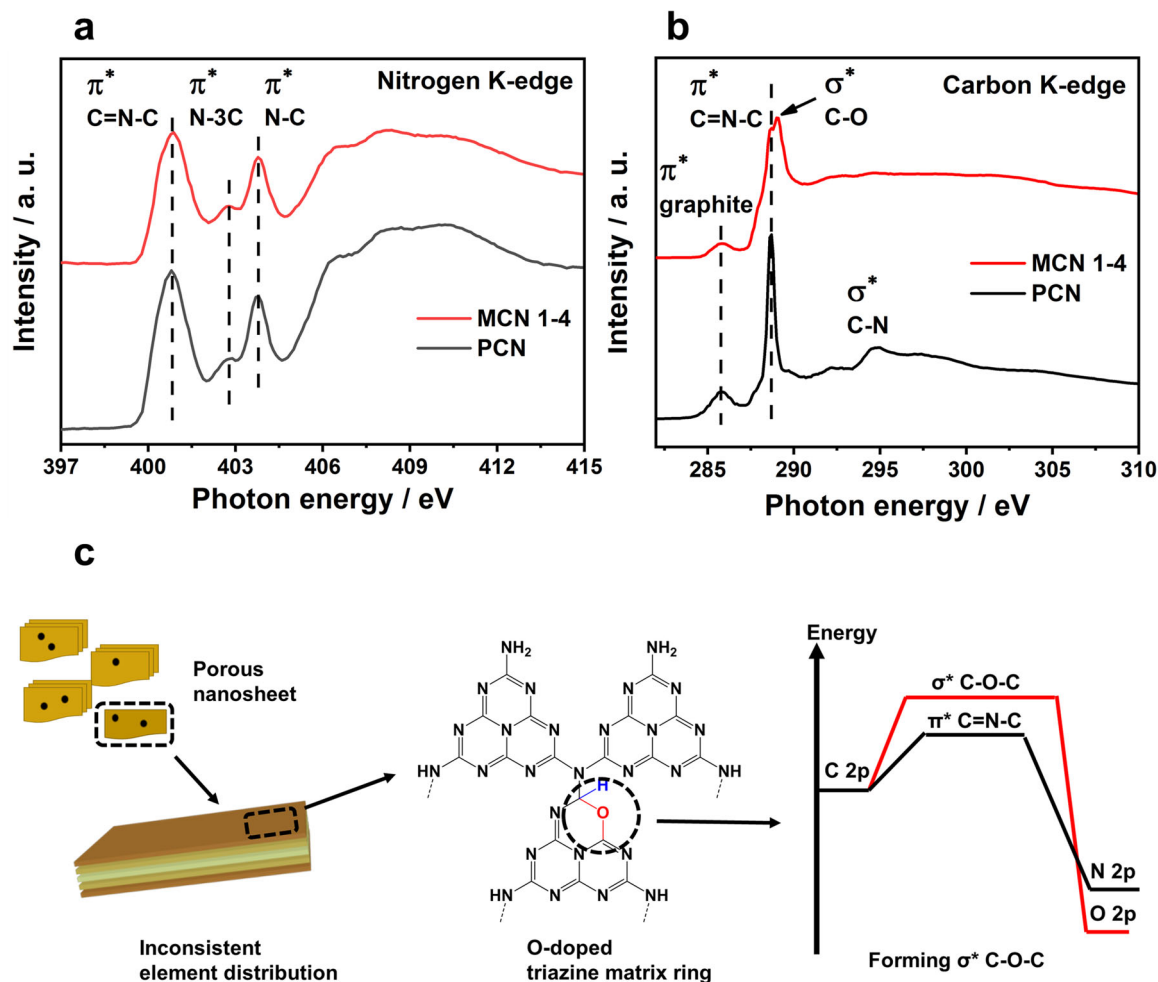


Fig. 6 NEXAFS characterization and schematic from structure to atomic orbital description of PCN and MCN1-4. NEXAFS spectra of PCN and MCN1-4 at the **a** nitrogen K-edge and **b** carbon K-edge. **c** Schematic description of covalent bonding in terms of atomic orbitals.

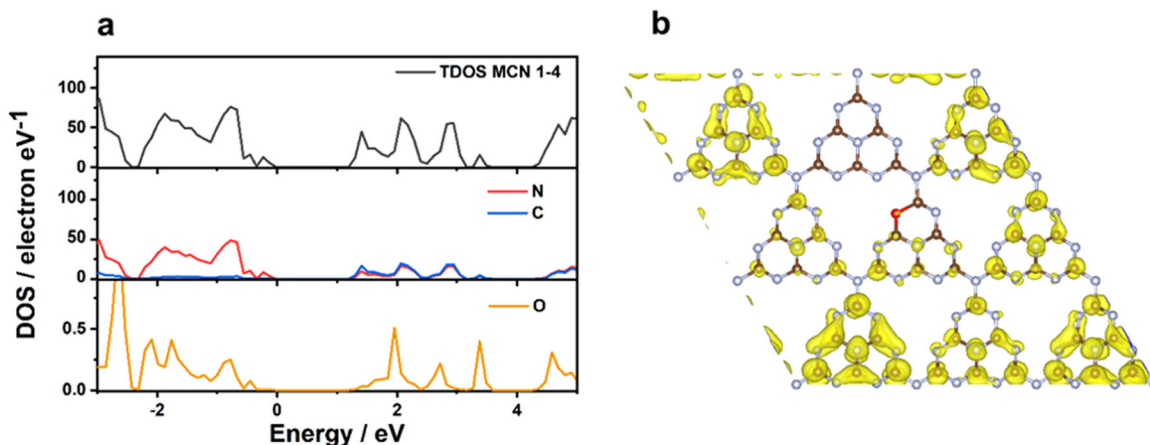


Fig. 7 Computational calculation of MCN1-4. **a** TDOS and PDOS of MCN1-4 and **b** the charge density of MCN1-4 derived from DOS at 1.33 eV. The Fermi level is set to zero.

density of states (PDOS) spectra of MCN1-4. It can be seen that the O atom starts to contribute to the conduction band from 1.31 eV near the conduction band edge (1.29 eV), and then reaches the maximum contribution at 1.95 eV. To further clarify the contribution of the σ^*_{C-O} in MCN1-4, we present charge density of MCN1-4 the orbital information associated with the

selected states in the TDOS of MCN1-4 (see Supplementary Fig. 26). As shown in Fig. 7b, a small amount of charge density can be observed on O atoms at 1.33 eV, which is only 0.05 eV higher than LUMO. The results demonstrate that the photo-generated electrons can be easily transferred to σ^*_{C-O} , which is consistent with the experimental results.

Discussion

To achieve a full spectrum response and a high activity, in addition to the upconversion properties of the carbon nitride due to defects, it is required that the lifetime of the photoexcited carriers should be sufficiently long. MCN1-4 has three features that result in a long photoexcited carrier lifetime: 1. O doped into the N position of the C=N-C moiety in the triazine matrix ring to form a σ^*_{C-O} orbital in conduction band and thus greatly inhibit the recombination of photoexcited electron-hole pairs; 2. a nanosheet morphology (3.5 nm) that provides not only a short distance for charge transfer from the interior of the material to the reaction site; 3. a gradual increase in the C content from the inside of the material to the surface, facilitating charge transfer from the inside to the surface (Fig. 6c). The latest reports on the development of infrared response photocatalysts have several shortcomings. For example, the photocatalysts achieve infrared light response at the expense of the activity under high-energy light irradiation; the photocatalysts must be compounded with other photocatalysts due to their low redox capacity. We believe that our strategy will open a brand-new approach for designing carbon nitride and other photocatalysts that can convert full-spectrum solar energy into chemical energy more efficiently. In addition, non-toxic C_3N_4 with high efficiency under infrared light provides a promising candidate for phototherapy.

Methods

Materials. Melamine (Aladdin, 99%), Cyanuric acid (Aladdin, 98%), Triethanolamine (Aladdin, AR-98%), TiO_2 (degussa, P25), TiO_2 (anatase, Macklin, 99.8%, 60 nm) and Hydrochloroplatinic acid (Alfa Aesar, ACS-99.95%, Pt 37.5%) were used as starting materials without further treatment. Deionized water (18.5 M Ω , EREE water systems) was used in the whole experiments.

Preparation of PCN and MCNx-y. Bulk C_3N_4 (polymeric carbon nitride, PCN) was synthesized by heating 3 g of melamine at 550 °C for 4 h, the heating rate is 5 °C min⁻¹.

Firstly, MCx-y was prepared by a facile hydrothermal treatment. Five grams of melamine and cyanuric acid composite (melamine/cyanuric acid are 2.5/2.5, 2/3, 1.5/3.5 and 1/4 weight ratio) was dispersed in 50 ml water by 15 min sonication and 15 min stirring. The suspension liquid was transferred into a 100 ml Teflon-lined autoclave and then heated at in an oven 150 °C for 6 h. After filtration and evaporation, a white powder was obtained, which was referred to as MCx-y (x and y are respectively denote as the added weight of melamine and cyanuric acid).

Then 3 grams of white powder was placed in an alumina crucible with a cover and heated to 550 °C in muffle furnace at a heating rate of ca. 5 °C min⁻¹. After heating at 550 °C for 4 h, MCNx-y was obtained. It is worth noting that the muffle furnace used in here should has a good thermal insulation.

Photocatalytic activity under infrared light irradiation. Fifty mg of sample was dispersed in 100 ml water (10 vol% of TEOA, and H_2PtCl_6 of 3 wt% Pt to the sample) for 10 min by sonication. The solution was transferred to the photocatalysis reactor, and vacuumed with stirred. Xe lamp (CEAULIGHT, CEL-HXF300, 300 W) with 420 cut-off filter (CEAULIGHT, CEL-UVIRCUT420) was used to irradiate the solution for 3 h (for Pt deposition). Subsequently, 800 cut-off filter (CEAULIGHT, CEL-UVIRCUT800) was used, the average light intensity was 24.4 mW cm⁻². The amounts of generated hydrogen were monitored by gas chromatography (TCD, CEAULIGHT, GC-7920) every 30 min. Ultrapure N_2 was used as the carrier gas. The reaction temperature was maintained 285 K by cycle water, unless otherwise noted.

Photocatalytic activity under visible light irradiation. Ten mg of sample was dispersed in 100 ml water (10 vol% of TEOA, and H_2PtCl_6 of 3 wt% Pt to the sample) for 10 min by sonication. The solution was transferred to the photocatalysis reactor, and vacuumed with stirred. A 300 W Xe lamp with 420 cut-off filter was used as the light source (the light intensity of the high position in the middle level of the liquid was 100 mW cm⁻²).

Photocatalytic activity under AM 1.5G irradiation. The same procedure was used as that under visible light, except that Xe lamp (300 W) with AM 1.5G filter (CEAULIGHT, CEL-AM1.5) was used as the light source (the light intensity of the high position in the middle level of the liquid was 100 mW cm⁻²).

Computational details. We investigated the DOS and PDOS of samples by using the Vienna Ab Initio Simulation Package (VASP)³⁷ based on density functional

theory (DFT). A large 3 × 3 supercell with perpendicular vacuum of 15 Å was used to eliminate the spurious interaction from the periodic. The generalized gradient approximation (GGA) as proposed by Perdew, Burke, and Ernzerhof (PBE)³⁸ considered the exchange-correlation functional, as well as the projector augmented wave (PAW) potentials. The lattice constants were set to a = b = 6.8 Å, all atoms were relaxed until the total energy converged to 10⁻⁵ eV and the residual force on each atom was less than 0.01 eV Å⁻¹. The plane-wave kinetic-energy cutoff was 450 eV and the grid mesh was 2 × 2 × 1.

Data availability

The authors declare that obtained and analyzed data are contained in the paper and the Supplementary Information, and are available from the corresponding author on reasonable request.

Received: 24 June 2020; Accepted: 28 October 2020;

Published online: 25 November 2020

References

- Hisatomi, T., Kubota, J. & Domen, K. Recent advances in semiconductors for photocatalytic and photoelectrochemical water splitting. *Chem. Soc. Rev.* **43**, 7520–7535 (2014).
- Wang, Z., Li, C. & Domen, K. Recent developments in heterogeneous photocatalysts for solar-driven overall water splitting. *Chem. Soc. Rev.* **48**, 2109–2125 (2019).
- Hernández-Alonso, M. D., Fresno, F., Suárez, S. & Coronado, J. M. Development of alternative photocatalysts to TiO_2 : challenges and opportunities. *Energy Environ. Sci.* **2**, 1231–1257 (2009).
- Maeda, K. & Domen, K. Photocatalytic water splitting: recent progress and future challenges. *J. Phys. Chem. Lett.* **1**, 2655–2661 (2010).
- Yang, M.-Q., Gao, M., Hong, M. & Ho, G. W. Visible-to-NIR photon harvesting: progressive engineering of catalysts for solar-powered environmental purification and fuel production. *Adv. Mater.* **30**, 1802894 (2018).
- Rahman, M. Z., Kwong, C. W., Davey, K. & Qiao, S. Z. 2D phosphorene as a water splitting photocatalyst: fundamentals to applications. *Energy Environ. Sci.* **9**, 709 (2016).
- Jiang, J. et al. Synthesis of visible and near infrared light sensitive amorphous titania for photocatalytic hydrogen evolution. *Green Chem.* **18**, 2056 (2016).
- Wang, X. et al. A metal-free polymeric photocatalyst for hydrogen production from water under visible light. *Nat. Mater.* **8**, 76–80 (2009).
- Zhao, F. et al. Supramolecular quantum dots as biodegradable nano-probes for upconversion-enabled bioimaging. *Chem. Commun.* **51**, 13201–13204 (2015).
- Zhang, X. et al. Single-layered graphitic- C_3N_4 quantum dots for two-photon fluorescence imaging of cellular nucleus. *Adv. Mater.* **26**, 4438 (2014).
- Liu, J. et al. Metal-free efficient photocatalyst for stable visible water splitting via a two-electron pathway. *Science* **347**, 970–974 (2015).
- Zhang, J.-W. et al. Oxygen-doped nanoporous carbon nitride via water-based homogeneous supramolecular assembly for photocatalytic hydrogen evolution. *Appl. Catal. B* **221**, 9–16 (2018).
- Zhen, W. et al. Efficient visible-light-driven selective oxygen reduction to hydrogen peroxide by oxygen-enriched graphitic carbon nitride polymers. *Energy Environ. Sci.* **11**, 2581 (2018).
- Wang, Y. et al. Linker-controlled polymeric photocatalyst for highly efficient hydrogen evolution from water. *Energy Environ. Sci.* **10**, 1643–1651 (2017).
- Wei, F. et al. Oxygen self-doped g- C_3N_4 with tunable electronic band structure for unprecedentedly enhanced photocatalytic performance. *Nanoscale* **10**, 4515–4522 (2018).
- Yu, Y. et al. Surface engineering for extremely enhanced charge separation and photocatalytic hydrogen evolution on g- C_3N_4 . *Adv. Mater.* **30**, 1705060 (2018).
- Ou, H. et al. Tri-s-triazine-based crystalline carbon nitride nanosheets for an improved hydrogen evolution. *Adv. Mater.* **29**, 1700008 (2017).
- Jürgens, B. et al. Melem (2,5,8-triamino-tri-s-triazine), an important intermediate during condensation of melamine rings to graphitic carbon nitride: synthesis, structure determination by X-ray powder diffractometry, solid-state NMR, and theoretical studies. *J. Am. Chem. Soc.* **125**, 10288–10300 (2003).
- Zhang, Q. et al. A photocatalytic degradation strategy of PPCPs by a heptazine-based CN organic polymer (OCN) under visible light. *Environ. Sci. Nano* **5**, 2325–2336 (2018).
- Jin, Z. et al. Hydrogen bonds in heterojunction photocatalysts for efficient charge transfer. *Appl. Catal. B* **234**, 198–205 (2018).

21. Jun, Y.-S. et al. From melamine-cyanuric acid supramolecular aggregates to carbon nitride hollow spheres. *Adv. Funct. Mater.* **23**, 3661–3667 (2013).
22. Shalom, M., Inal, S., Fettkenhauer, C., Neher, D. & Antonietti, M. Improving carbon nitride photocatalysis by supramolecular preorganization of monomers. *J. Am. Chem. Soc.* **135**, 7118–7121 (2013).
23. Haase, M. & Schafer, H. Upconverting nanoparticles. *Angew. Chem., Int. Ed.* **50**, 5808–5829 (2011).
24. Ren, C. et al. A near-infrared I emissive dye: toward the application of saturable absorber and multiphoton fluorescence microscopy in the deep-tissue imaging window. *Chem. Comm.* **55**, 5111–5114 (2019).
25. Lau, V. W.-h. et al. Rational design of carbon nitride photocatalysts by identification of cyanamide defects as catalytically relevant sites. *Nat. Commun.* **7**, 12165 (2016).
26. Kudo, A. & Miseki, Y. Heterogeneous photocatalyst materials for water splitting. *Chem. Soc. Rev.* **38**, 253–278 (2009).
27. Huang, S. et al. Non-precious molybdenum nanospheres as a novel cocatalyst for full-spectrum-driven photocatalytic CO₂ reforming to CH₄. *J. Hazard. Mater.* **393**, 122324–122330 (2020).
28. Yuan, J. et al. Crystallization, cyanamide defect and ion induction of carbon nitride: exciton polarization dissociation, charge transfer and surface electron density for enhanced hydrogen evolution. *Appl. Catal. B* **251**, 206–212 (2019).
29. Godin, R., Wang, Y., Zwijnenburg, M. A., Tang, J. & Durrant, J. R. Time-resolved spectroscopic investigation of charge trapping in carbon nitrides photocatalysts for hydrogen generation. *J. Am. Chem. Soc.* **139**, 5216–5224 (2017).
30. Corp, K. L. & Schlenker, C. W. Ultrafast spectroscopy reveals electron-transfer cascade that improves hydrogen evolution with carbon nitride photocatalysts. *J. Am. Chem. Soc.* **139**, 7904–7912 (2017).
31. Liang, L. et al. Infrared light-driven CO₂ overall splitting at room temperature. *Joule* **2**, 1004–1016 (2018).
32. Wang, H. et al. Oxygen-vacancy-mediated exciton dissociation in BiOBr for boosting charge-carrier-involved molecular oxygen activation. *J. Am. Chem. Soc.* **140**, 1760–1766 (2018).
33. Zheng, Y. et al. Hydrogen evolution by a metal-free electrocatalyst. *Nat. Commun.* **5**, 3783 (2014).
34. Zhang, G. et al. Tailoring the grain boundary chemistry of polymeric carbon nitride for enhanced solar hydrogen production and CO₂ reduction. *Angew. Chem., Int. Ed.* **58**, 3433–3437 (2019).
35. Kuznetsova, A. et al. Oxygen-containing functional groups on single-wall carbon nanotubes: NEXAFS and vibrational spectroscopic studies. *J. Am. Chem. Soc.* **123**, 10699–10704 (2001).
36. Atkins, P., Jones, L. & Laverman, L. *Chemical Principles. The Quest for Insight*, 6th ed. 2005, (W.H. Freeman & Company Press).
37. Kress, G. & Furthmüller, J. Efficiency of ab-initio total energy calculations for metals and semiconductors using a plane-wave basis set. *Comput. Mater. Sci.* **6**, 15–50 (1996).
38. Kress, G. & Furthmüller, J. Efficiency iterative schemes for ab initio total-energy calculations using a plane-wave basis set. *Phys. Rev. B* **54**, 11169–11186 (1996).

Acknowledgements

This work was supported by the Shenzhen Science and Technology Project under Grant Nos. JCYJ20170412105400428 and JCYJ20180507182246321, the Shenzhen Peacock Technological Innovation Project under Grant No. KQJSCX20170727101208249, the National Natural Science Foundation of China under Grant No. 21805191. Near Edge X-ray Absorption Fine Structure (NEXAFS) were carried out at the Catalysis and Surface Science Endstation at the BL11U beamline in the National Synchrotron Radiation Laboratory (NSRL) in Hefei, China. The authors thank the technical support from The Photonics Centre of Shenzhen University.

Author contributions

Z.J. conceived the idea and conducted the experiments. X.J. conducted the TAS measurement. Q.Z. measured and analyzed NEXAFS. Z.J., S.H., and L.Z. discussed the experiment detail. T.H. conducted open-aperture the Z-scan measurement. L.H. conducted computational calculation. Y.Z., H.Z., and S.R. supervised the experimental work. Z.J., T.O., and Y. Z. discussed the results and wrote the paper with contributions from the other authors.

Competing interests

The authors declare no competing interests.

Additional information

Supplementary information is available for this paper at <https://doi.org/10.1038/s43246-020-00093-z>.

Correspondence and requests for materials should be addressed to Y.-J.Z.

Peer review information Primary handling editor: John Plummer

Reprints and permission information is available at <http://www.nature.com/reprints>

Publisher's note Springer Nature remains neutral with regard to jurisdictional claims in published maps and institutional affiliations.



Open Access This article is licensed under a Creative Commons Attribution 4.0 International License, which permits use, sharing, adaptation, distribution and reproduction in any medium or format, as long as you give appropriate credit to the original author(s) and the source, provide a link to the Creative Commons license, and indicate if changes were made. The images or other third party material in this article are included in the article's Creative Commons license, unless indicated otherwise in a credit line to the material. If material is not included in the article's Creative Commons license and your intended use is not permitted by statutory regulation or exceeds the permitted use, you will need to obtain permission directly from the copyright holder. To view a copy of this license, visit <http://creativecommons.org/licenses/by/4.0/>.

© The Author(s) 2020